Contents lists available at SciVerse ScienceDirect

Applied Catalysis B: Environmental

Supported CeO$_2$ catalysts in technical form for sustainable chlorine production

M. Moser [a], C. Mondelli [a], T. Schmidt [b], F. Girgsdies [c], M.E. Schuster [c], R. Farra [c],
L. Szentmiklósi [d], D. Teschner [c,d], J. Pérez-Ramírez [a,*]

[a] Institute for Chemical and Bioengineering, Department of Chemistry and Applied Biosciences, ETH Zurich, Wolfgang-Pauli-Strasse 10, CH-8093 Zurich, Switzerland
[b] Bayer MaterialScience AG, IO-BC-PI, Chempark B537, D-41538 Dormagen, Germany
[c] Fritz-Haber-Institute of the Max Planck Society, Faradayweg 4-6, D-14159 Berlin, Germany
[d] Centre for Energy Research, Hungarian Academy of Sciences, Budapest H-1525, Hungary

ARTICLE INFO

ABSTRACT

Bulk CeO$_2$ has been recently reported as a promising catalyst for the oxidation of HCl to Cl$_2$. In order to undertake the scale up of this system, various oxides (TiO$_2$, Al$_2$O$_3$, and low- and high-surface area ZrO$_2$) have been evaluated as carriers. Supported CeO$_2$ catalysts (3–20 wt.% Ce) prepared by dry impregnation were isothermally tested at the lab scale. Their performance was ranked as: CeO$_2$/ZrO$_2$ $\gg$ CeO$_2$/Al$_2$O$_3$ $\geq$ CeO$_2$/TiO$_2$. Kinetic data revealed a lower activation energy and a similar activity dependence on the partial pressure of O$_2$ for CeO$_2$/ZrO$_2$ compared to bulk CeO$_2$. Pilot-scale testing over 3-mm pellets of this catalyst evidenced outstanding stability for 700 h on stream. In-depth characterization of the carriers and fresh catalysts by N$_2$ sorption, Hg porosimetry, X-ray diffraction, temperature-programmed reduction with H$_2$, Raman spectroscopy, electron microscopy, and *in situ* prompt gamma activation analysis, enabled to rationalize the different catalytic behavior of the materials. ZrO$_2$ stabilizes nanostructures of CeO$_2$ and a Ce–Zr mixed oxide phase, which offer high dispersion and improved oxidation properties. The catalyst also shows reduced chlorine uptake, and overall stands as a better Deacon material compared to bulk CeO$_2$ and other supported systems. CeO$_2$ is present on Al$_2$O$_3$ predominantly as well-distributed nanoparticles. Still, alumina does not induce any electronic effect, thus the supported phase behaves similarly to bulk ceria. TiO$_2$, likely due to the structural collapse and dramatic sintering suffered during calcination, leads to the formation of very large ceria particles. Based on our results, CeO$_2$/ZrO$_2$ appears as a robust and cost-effective alternative to the current RuO$_2$-based catalysts for large-scale chlorine recovery.

© 2012 Elsevier B.V. All rights reserved.

1. Introduction

The rapidly increasing production of polyurethanes and polycarbonates determines a rising excess of by-product HCl. The polyvinyl chloride manufacture cannot absorb the HCl surplus anymore, as the demand for this polymer grows at a slower pace than that of the above-mentioned plastics. In this scenario, as HCl neutralization is an environmentally unattractive option and marketing as hydrochloric acid is not always feasible, recycling represents a sustainable strategy to valorize the HCl excess. To this end, the heterogeneously catalyzed oxidation of HCl to Cl$_2$ (Deacon reaction) comprises a preferential route with respect to the conventional HCl electrolysis in view of the unbeatably lower energy demand [1]. At present, the state-of-the-art industrial catalysts for this reaction are based on RuO$_2$, featuring remarkable low-temperature activity and lifetime [2,3]. Nevertheless, as ruthenium is a pricey

metal, research efforts have been oriented towards the identification of cost-effective but equally stable alternatives. Ceria (CeO$_2$) has been found significantly active in HCl oxidation owing to the presence of oxygen vacancies in the material [4]. Bulk chlorination only occurred at feed O$_2$/HCl < 0.75, leading to the formation of CeCl$_3$ and to activity loss, although exposure to O$_2$-rich conditions enabled to rapidly and fully restore the active oxide phase. Recent studies have revealed that rejuvenation of chlorinated ceria limitedly to the outermost surface layers is sufficient to recover the original activity level and that even bulk CeCl$_3$ can be completely transformed into CeO$_2$ at O$_2$/HCl > 4 and 703 K [5]. The negative impact of high Cl coverages on the activity was attributed to the more difficult vacancy formation [5].

These results with bulk CeO$_2$ triggered further work regarding the selection of a suitable support for this active phase. The morphological and electronic properties of ceria and, thus, its performance, can be tuned using carriers of different textural, structural, and chemical nature [6]. This would enable the establishment of property–function relationships and the attainment of an optimized material. In fact, this is the logical step towards the scale up

* Corresponding author. Tel.: +41 44 633 7120; fax: +41 44 633 1405.
 E-mail address: jpr@chem.ethz.ch (J. Pérez-Ramírez).

of a technical catalyst. Although CeO_2 has been commonly applied as a support or cocatalyst [7–19], a few supported ceria catalysts have been reported in the literature. For instance, $CeO_2/\gamma-Al_2O_3$ has been used for SO_x removal [20], VOC oxidation [21], and, in combination with noble metals, for exhaust after-treatment [6]. It has been found that, at low loadings, ceria is stabilized on alumina in form of well-distributed nanostructures [22], and that a high ceria dispersion can be attained even upon high-temperature calcination, as Ce incorporation prevents the alumina transformation from the γ- into the α-form and thus surface area loss [23]. In view of these results and of its resistance against chlorination, γ-alumina was selected as a potential carrier. Zirconia has been widely applied in exhaust after-treatment catalysts, too, though usually in the form of solid solutions with ceria rather than as a conventional support [6,24]. Mixed Cr–Zr oxidic phases possess superior thermal stability, and, more interestingly, improved oxygen storage capacity compared to pure ceria [24–27]. Due to these features, zirconia stands as a likely suitable carrier for ceria. Titania was also selected in view of its high surface area and wide availability.

Herein, supported CeO_2 catalysts, synthesized by dry impregnation of cerium nitrate on the above-mentioned carriers, have been evaluated in HCl oxidation at the laboratory scale. Structure, dispersion, and electronic properties of ceria were assessed by extensive characterization to explain the observed influence of the carrier on the performance. Long-term pilot tests of the most promising CeO_2-based catalyst in technical form provide excellent perspectives to supplement RuO_2-based catalysts for HCl recycling.

2. Experimental

2.1. Catalysts

$\gamma-Al_2O_3$ (99.95%), TiO_2-anatase (99.7%), as well as low- and high-surface area monoclinic ZrO_2 (both 99.8%, denoted with the suffixes "1" and "2", respectively), were provided by Saint-Gobain NorPro in pelletized form (diameter = 3 mm, length = 4 mm). The shaped materials were crushed, sieved, and dried in air at 433 K and 100 mbar for 2 h prior to their use. Supported CeO_2 catalysts (3–20 wt.% Ce) were prepared by dry impregnation of these supports with an aqueous solution of $Ce(NO_3)_3 \cdot 6H_2O$ (Sigma–Aldrich, 99.99%), followed by drying in air at 353 K and 100 mbar for 5 h and calcination in static air at 1173 K (3 K min^{-1}) for 5 h. This calcination temperature was found optimal for bulk CeO_2 in HCl oxidation [4]. The as-prepared catalysts are referred to as fresh. For long-term testing at the pilot scale, CeO_2/ZrO_2-1 (9 wt.% Ce), prepared by dry impregnation of cylindrical ZrO_2-1 pellets (diameter = 3 mm, length = 4 mm), were used.

2.2. Characterization

The cerium loading was determined by inductively coupled plasma-optical emission spectroscopy (ICP-OES) in a Horiba Jobin Yvon Ultima 2 instrument after dissolution of the catalysts in a $HF/HCl/HNO_3$ solution. Nitrogen sorption at 77 K was measured in a Quantachrome Quadrasorb-SI analyzer. Prior to the analysis, the samples were evacuated at 473 K for 10 h. The Brunauer–Emmett–Teller (BET) method was applied to calculate the total surface area. Mercury porosimetry (MP) was carried out in a Micromeritics Autopore IV 9510 analyzer. After degassing the samples, mercury was intruded in the pressure range from vacuum to 418 MPa. Measurements were performed using a contact angle of 140° for mercury and a pressure equilibration time of 10 s. The Washburn equation was applied to calculate the pore size distribution. X-ray diffraction (XRD) was carried out in a Bruker AXS D8 Advance theta/theta diffractometer equipped with a secondary graphite monochromator ($CuK\alpha_{1+2}$ radiation) and a scintillation detector. Data were collected in the 5–70 2θ range with an angular step size of 0.02° and a counting time of 15 s per step. The full XRD patterns were fitted to evaluate the contributions of the individual phases according to the Rietveld method, in conjunction with the fundamental parameters approach [28] for the instrumental and double-Voigt approach [29]. The crystallite domain sizes of relevant phases, as obtained from the double-Voigt model, were given as L_{Vol} – IB values (volume weighed mean column lengths based on integral breadth), *i.e.* without further assumptions about crystallite size or shape distribution. Temperature-programmed reduction with hydrogen (H_2-TPR) was measured in a Thermo TPDRO 1100 unit with a thermal conductivity detector. Samples were pre-treated in He (20 cm^3 STP min^{-1}) at 473 K for 30 min. After cooling to 323 K in He, the analysis was carried out in 5 vol.% H_2/N_2 (20 cm^3 STP min^{-1}), ramping the temperature from 323 to 1173 K at 10 K min^{-1}. Raman spectroscopy was measured in a Renishaw inVia Raman microscope equipped with a coherent argon-ion laser (20 mW, 514 nm) and a high sensitivity ultra-low noise CCD detector. Spectra were collected between 1400 and 24 cm^{-1} accumulating 10 scans with a resolution of 1 cm^{-1}. The total exposure time of each sample was 8 s. The spectra were fitted in the 520–420 cm^{-1} range by means of Gauss–Lorentz functions. Bright-field and dark-field transmission electron microscopy (BF/DFTEM) studies were carried out in a Philips CM 200 FEG and a FEI Titan Cs 80–300 microscope, equipped with a FEG, a Gatan Tridiem Filter, and an energy-dispersive X-ray (EDX) analyzer, and operated at 200 and 300 keV, respectively. In the case of the Titan microscope, spherical aberrations were corrected by the CEOS Cs-corrector, thus reaching an information limit of 0.8 Å. High-resolution TEM (HRTEM) images were processed to obtain the power spectra which were used to measure interplanar distances and angles for phase identification. Energy-filtered TEM (EFTEM) and Electron Energy-Loss Spectroscopy (EELS) maps were acquired in the FEI microscope with the post-column Gatan Tridiem Filter. Scanning TEM images were obtained with a high-angle annular dark field detector (HAADF STEM).

2.3. In situ prompt gamma activation analysis

In situ prompt gamma activation analysis (PGAA) was used to assess the Cl uptake of selected supported ceria samples during HCl oxidation and its effect on the reactivity. The method, successfully used to study the surface chlorination of Deacon catalysts [5,30], is based on the neutron caption of the sample and the subsequent detection of element-specific gamma rays during de-excitation of the nuclei. PGAA was carried out under atmospheric pressure at the cold neutron beam of the Budapest Neutron Centre. A Compton-suppressed high-purity germanium crystal was used to detect the prompt gamma photons. Cl and Ce were quantified in the investigated volume, *i.e.* a tubular micro-reactor. Molar ratios (Cl/Ce) were determined from the characteristic peak areas corrected by the detector efficiency and the nuclear data of the observed elements. The gas-phase Cl signal (HCl, Cl_2) was subtracted, thus, all Cl/Ce ratios reported correspond only to the solid catalyst. The quartz reactor (8 mm i.d.) was loaded with 0.5–0.7 g of catalyst (W_{cat}) of particle size = 0.1–0.25 mm, placed into the neutron beam, and surrounded by a specially designed oven having openings for the incoming and outgoing neutrons and for the emitted gamma rays. These openings were covered by thin aluminum foils to minimize heat losses. The reaction feed was supplied by mass flow controllers at a constant total volumetric flow (F_T) of 166.6 cm^3 STP min^{-1}, and was composed by 10 vol.% HCl (Linde, purity 4.5) and variable amounts of O_2 (Linde, purity 5.0), balanced with N_2 (Linde, purity 5.0). The Cl uptake was monitored at 703 K and variable

Table 1
Characterization and activity data of selected supported CeO_2 catalysts with 7 wt.% Ce.

Sample	S_{BET}[a]/$m^2\,g^{-1}$	Ce/wt.%	STY[b]/g Cl_2 g_{cat}^{-1} h^{-1}	
			After 5 h	After 23 h
CeO_2/Al_2O_3	165 (242)	6.0	0.48	0.45
CeO_2/TiO_2	8 (111)	6.3	0.40	0.38
CeO_2/ZrO_2-1	42 (47)	6.8	1.23	1.19
CeO_2/ZrO_2-2	29 (89)	6.3	0.80	0.76

[a] Surface area of the as-received carriers in brackets.
[b] Conditions: $W_{cat} = 0.25$ g, $O_2/HCl = 4$, and $T = 703$ K.

O_2/HCl ratio (0.5 to 9) or at $O_2/HCl = 9$ and variable temperature (643–703 K).

2.4. Catalytic tests in lab and pilot reactors

The gas-phase oxidation of hydrogen chloride was studied in a quartz fixed-bed micro-reactor (8 mm i.d.) at ambient pressure. 0.25–0.7 g of catalyst (particle size = 0.1–0.25 mm), diluted with 1 g of glass spheres (>400 μm), were loaded in the reactor and pre-treated in flowing N_2 at 703 K for 30 min. Thereafter, the reaction mixture, 10 vol.% HCl (Linde, purity 4.5), 40 vol.% O_2 (Linde, purity 4.5), and 50 vol.% N_2 (Linde, purity 5.0), was continuously fed. The steady-state activity of the catalysts was measured isothermally using a bed temperature (T_{bed}) of 703 K and a total volumetric flow of 166 cm^3 STP min^{-1} for 23 h on stream. Kinetic data were obtained upon variation of the O_2/HCl ratio in the range of 0.5–9 at 703 K and of the temperature in the range of 643–703 K at $O_2/HCl = 9$. Long-term stability tests were conducted over CeO_2 (9 wt.% Ce)/ZrO_2 pellets (diameter = 3 mm, length = 4 mm) in a pilot plant consisting of an adiabatic reactor ($T_{inlet} = 633$ K) at Bayer MaterialScience. The feed O_2/HCl ratio was kept constant at 4.15. In all the *in situ* PGAA and the catalytic tests, Cl_2 quantification was carried out by iodometric titration [31]. The catalytic activity was assessed by determining the HCl conversion, defined as $X_{HCl} = (2 \times$ mole Cl_2 at the reactor outlet/mole HCl at the reactor inlet) × 100%, and the space time yield (STY), defined as the gram of Cl_2 produced per gram of catalyst and per hour. For the pilot test, the HCl conversion was additionally measured at 10% of the total catalyst bed length. The Weisz–Prater criterion was largely fulfilled in all our lab-catalytic tests, indicating the absence of intra-particle diffusion limitations.

3. Results and discussion

3.1. Catalysis

Alumina-, titania-, and zirconia-supported CeO_2 catalysts (nominal 7 wt.% Ce) were tested in HCl oxidation for 23 h on stream. The Cl_2 production of all catalysts was essentially constant in the evaluated time frame (Table 1). The catalysts were ranked according to their activity as follows: CeO_2/ZrO_2-1 > CeO_2/ZrO_2-2 ≫ CeO_2/Al_2O_3 ≥ CeO_2/TiO_2. Due to the structural collapse of TiO_2 upon calcination of the impregnated catalyst (*vide infra*), only ZrO_2-1, ZrO_2-2, and Al_2O_3 were considered for the optimization of the cerium content. Catalysts with loadings between 3 and 20 wt.% Ce were prepared and tested for 5 h on stream (Fig. 1). The optimal Ce loading on ZrO_2-1 and ZrO_2-2 was reached between 7 and 10 wt.%, as a further increase in metal content did not lead to an enhanced space time yield. Within this loading range, CeO_2/ZrO_2-1 exhibited a better performance than CeO_2/ZrO_2-2. In the case of CeO_2/Al_2O_3, the activity increased linearly with the Ce loading up to 17 wt.% Ce. Only at this loading, the alumina-supported catalyst exhibited comparable activity to the zirconia-supported samples. Zirconia appears as the preferred carrier not only in view of the beneficial
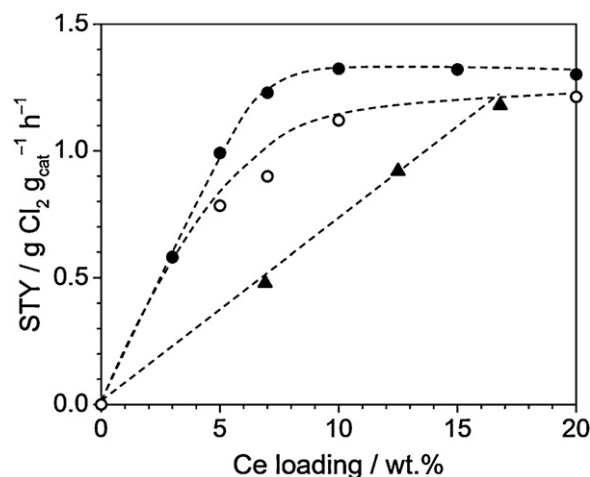

Fig. 1. Space time yield after 5 h on stream *versus* Ce loading over CeO_2/ZrO_2-1 (solid circles), CeO_2/ZrO_2-2 (open circles), and CeO_2/Al_2O_3 (solid triangles). Conditions: $W_{cat} = 0.25$ g, $O_2/HCl = 4$, and $T = 703$ K.

effect on the specific catalytic activity but also due to the high density of the material. With an equal cerium loading, CeO_2/ZrO_2 requires a three times smaller bed volume than CeO_2/Al_2O_3. This enables the use of a smaller reactor and thus reduction of capital investment costs, which represent one major challenge of the catalytic chlorine recovery technology [1].

Kinetic investigations were performed on CeO_2/ZrO_2-1 (7 wt.% Ce) and CeO_2/Al_2O_3 (12.2 wt.% Ce). In the case of the zirconia-supported catalyst, the feed O_2/HCl ratio was varied from 0.5 to 9 at 703 K (Fig. 2a). According to power equation fitting of the data, the reaction order on oxygen is 0.4, resembling previous findings on bulk CeO_2 [4]. The dependence of the HCl conversion on the bed temperature was explored at 643–703 K keeping a $O_2/HCl = 9$ (Fig. 2b). The apparent activation energy was estimated at 60 kJ mol^{-1}, This value is significantly lower than the 90 kJ mol^{-1} originally reported for bulk CeO_2 [4] and the 70–75 kJ mol^{-1} more recently obtained for the pure oxide through refined experiments [5]. This is later explained based on a reduced Cl coverage in the supported catalyst. The effect of varying the partial pressure of O_2 was evaluated for CeO_2/Al_2O_3 using two protocols: starting with a high oxygen excess and step-wise decreasing the oxygen content, and *vice versa* (Fig. 2a). The downward series gave rise to a power law dependence, which rendered a reaction order of 0.6, whereas the upward series resulted in an essentially linear correlation with a lower activity. This discrepancy will be rationalized on the basis of different chlorination degrees (*vide infra*).

The most active catalyst, CeO_2/ZrO_2-1 (9 wt.% Ce), was tested in technical form in a pilot plant to assess its long-term stability. Fig. 3 shows that the HCl conversion levels measured using a probe at 10% of the bed length and at the reactor outlet were constant for over 700 h on stream. Monitoring the activity along the bed helps to assess the catalyst robustness. In fact, common causes of deactivation for Deacon catalysts are chlorination by HCl, inhibition by Cl_2, and sintering. The latter two might affect the catalyst to larger extent close to the outlet of the adiabatic reactor, where the concentration of Cl_2 is the highest and the temperature normally reaches its maximum, but chlorination by HCl is expected to be predominant at the reactor inlet where the O_2/HCl ratio is the lowest. On the basis of its remarkable activity and lifetime, CeO_2/ZrO_2-1 comprises a realistic alternative to RuO_2-based catalysts for large-scale chlorine recycling.
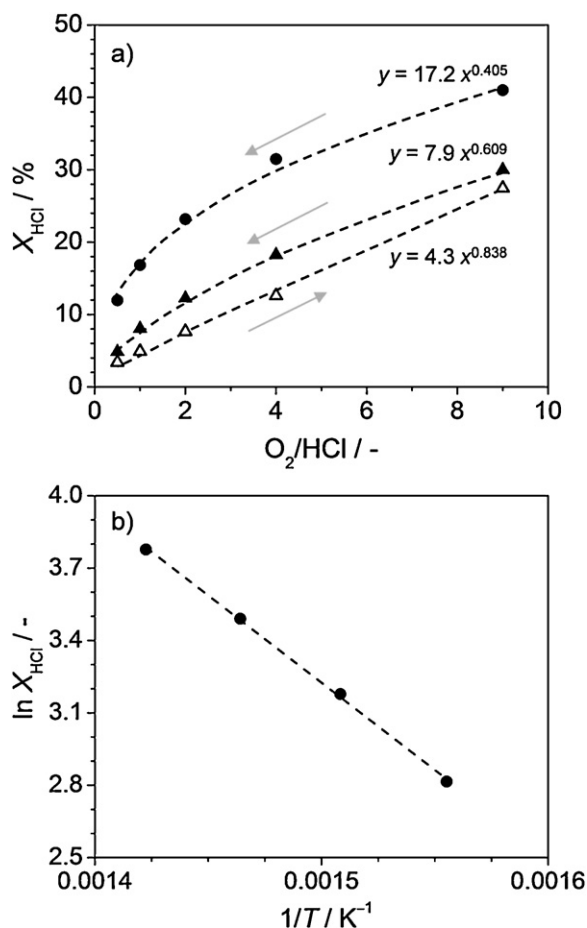
Fig. 2. (a) HCl conversion *versus* O_2/HCl ratio over CeO_2/ZrO_2-1 (downwards, solid circles) and CeO_2/Al_2O_3 (upwards, open triangles; downwards, solid triangles). Conditions: W_{cat} = 0.5 g, T = 703 K. (b) Arrhenius plot for CeO_2/ZrO_2-1. Conditions: W_{cat} = 0.7 g and O_2/HCl = 4.

3.2. Characterization

The carriers and the supported catalysts have been characterized in fresh form by means of various techniques in order to
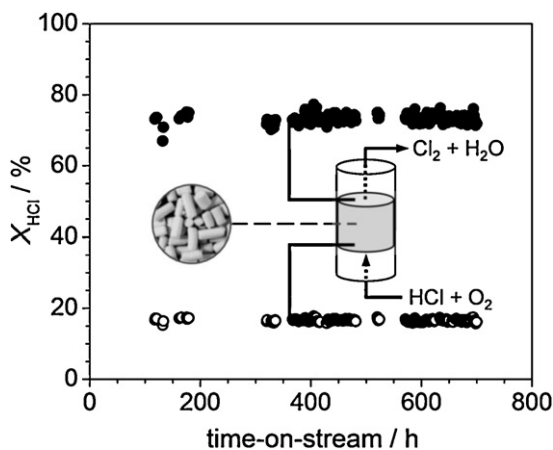

Fig. 3. HCl conversion at 10% of the total catalyst bed length (open circles) and at the reactor outlet (solid circles) over CeO_2/ZrO_2-1 (9 wt.% Ce) pellets during a long-term test in a pilot plant. Conditions: pellet diameter = 3 mm, O_2/HCl = 4.15, T_{inlet} = 633 K, and P = 1 bar. The inset shows a schematic representation of the fixed-bed reactor and the sampling points (right) and a photograph of the technical CeO_2/ZrO_2-1 catalyst (left).
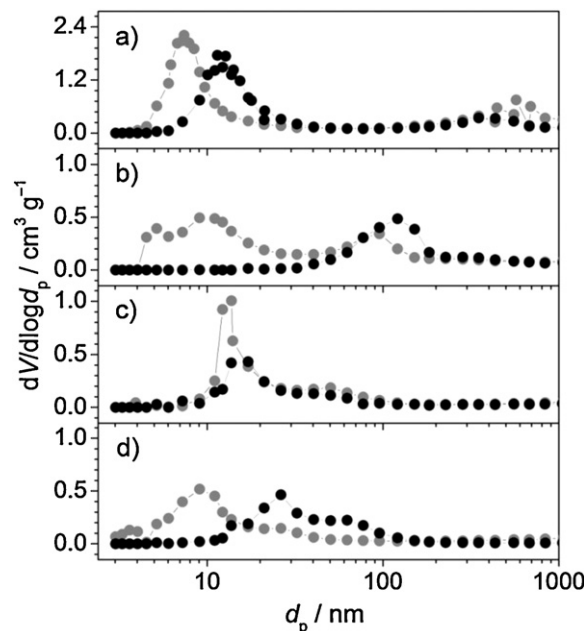

Fig. 4. Pore size distributions obtained from Hg porosimetry of the carriers (grey circles) and the supported CeO_2 catalysts with 7 wt.% Ce (black circles): (a) Al_2O_3, (b) TiO_2, (c) ZrO_2-1, and (d) ZrO_2-2.

rationalize the differences in catalytic performance. The actual loading of Ce was determined by elemental analysis and found to be slightly lower than the nominal 7 wt.% for all of the catalysts (Table 1). The total surface area (S_{BET}) of the as-received supports was 47, 89, 111, and 242 m^2 g^{-1} for ZrO_2-1, ZrO_2-2, TiO_2, and Al_2O_3, respectively (Table 1). The original S_{BET} of ZrO_2-1 was retained upon CeO_2 deposition. On the contrary, it decreased to a significant extent for Al_2O_3 and ZrO_2-2, and dramatically for TiO_2, suggesting particle sintering and/or pore blockage upon catalyst preparation. The pore size distributions of the carriers and supported CeO_2 catalysts are reported in Fig. 4. Al_2O_3 possessed mesopores of 4–15 nm size and macropores in the range of 300–900 nm (Fig. 4a). The CeO_2/Al_2O_3 profile evidences a nearly complete loss of the original support mesopores, the appearance of mesoporosity at 10–20 nm, and the partial depletion of the macropores. As CeO_2 is mainly present in form of small nanoparticles (*vide infra*) and S_{BET} drops, the change in porous structure is supposed to be related to pore blockage by the active phase as well as to thermal ageing induced by the high-temperature calcination after the impregnation step. Titania featured pores in the range of 4–200 nm, where mesopores of 5–10 nm and macropores of 70–110 nm size are most abundant. These mesopores were completely lost upon catalyst preparation, whereas porosity developed to some extent in the 60–200 nm range (Fig. 4b). In line with the almost complete depletion of the S_{BET}, these observations are later explained on the basis of pronounced structural alterations occurring during the thermal activation. In the case of ZrO_2-1, the pores between 10 and 20 nm partially vanished after impregnation of the Ce precursor and calcination, but the larger pores (up to 100 nm) were mostly retained (Fig. 4c). ZrO_2-2 presented pores in the range of 4–40 nm with a predominance of pores of 4–10 nm. The deposition of the active phase led to the loss of the pores <10 nm, an increment of the larger ones, and the formation of even bigger pores (up to 100 nm) (Fig. 4d). Similar porosity changes were reported for mixed ceria-zirconia materials upon thermal treatments under reducing or oxidative atmospheres [32].

The availability of a large support surface is usually favorable to attain a high dispersion of the supported active phase, which
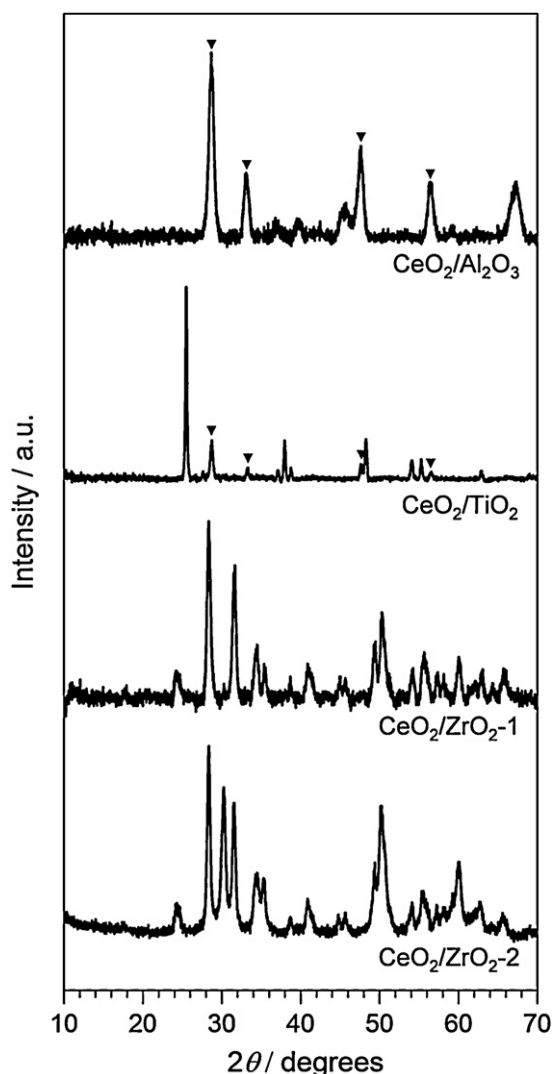
Fig. 6. Enlarged view of the 20–40°2θ range of the XRD pattern of (a) ZrO_2-1, (b) CeO_2/ZrO_2-1, (c) ZrO_2-2, and (d) CeO_2/ZrO_2-2 (solid lines) and fitting curves for monoclinic and tetragonal ZrO_2 (dashed and dash-dotted line, respectively), and cubic CeO_2 phases (short-dotted line), calculated by the Rietveld method. Weight fractions of the phases detected are indicated.

Fig. 5. XRD patterns of the supported CeO_2 catalysts. The following phases were detected: γ-Al_2O_3 (ICDD PDF-2 00-56-0457), TiO_2-anatase (ICDD PDF-2 01-71-1166), monoclinic ZrO_2 (ICDD PDF-2 01-078-0047), tetragonal ZrO_2 (ICDD PDF-2 01-072-7115), and cubic CeO_2 (ICDD PDF-2 01-73-6328). The reflections marked with solid triangles belong to CeO_2.

typically leads to enhanced activity. However, this is not the case here, as the catalysts' activity trend does not correlate to that of the S_{BET} data. Thus, the carrier nature seems to play a strong role in defining the specific character of the active ceria phase. Furthermore, as hinted by the changes in the porosity during catalyst preparation, their structural stability may be also relevant. The XRD patterns of the fresh catalysts are shown in Fig. 5. For the alumina-supported system, diffraction lines specific to cubic CeO_2 and γ-Al_2O_3 are visible. Comparison with the XRD pattern of the pure support indicates that the structure of γ-alumina was retained upon deposition of the Ce, in line with the studies by Damyanova et al. [23]. Indications on changes of crystallinity cannot be easily extracted, as the alumina peaks are rather broad and weak, due to the pseudo-amorphous nature of the small alumina crystallites. Ceria is also clearly identified in the diffractogram of CeO_2/TiO_2, along with the TiO_2-anatase phase. The clearly sharper support reflections in the catalyst pattern with respect to that of pure TiO_2 indicate a largely increased crystallinity, explained by sintering, as anticipated above. The absence of additional peaks related to TiO_2-rutile allows excluding that this structural alteration was provoked by an incipient phase transition, which is thermodynamically
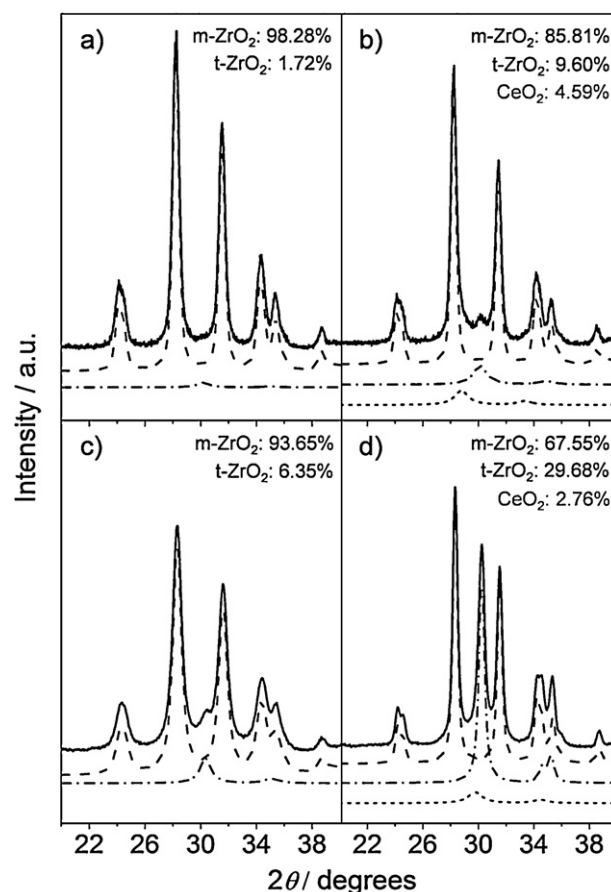
feasible at the temperature applied for the calcination but can be hindered by the presence of Ce [33,34], thus pointing to a thermal effect. For the ZrO_2-1- and ZrO_2-2-supported catalysts, the ceria phase was visualized only upon Rietveld fitting of the patterns and evaluated to represent about 3–5 wt.% of the samples (Fig. 6). This suggests that the ceria phase might be present in form of smaller nanostructures on the zirconia carriers with respect to alumina and titania. The fitting procedure also indicated that the original supports were almost entirely constituted by monoclinic zirconia with minor contributions from tetragonal zirconia (ca. 2 and 6 wt.% for ZrO_2-1 and ZrO_2-2, respectively). The deposition of ceria provoked a 5-fold increase of the amount of tetragonal zirconia in both cases. The tetragonal zirconia phase of ZrO_2-2 (equal to ca. 30 wt.% in CeO_2/ZrO_2-2) is clearly discernible in the XRD pattern of the fresh catalyst. The lattice parameters of both monoclinic and tetragonal zirconia show no clear indication of cerium doping in the catalysts. Still, the insertion of low Ce amounts into the zirconia lattice would produce a hardly discernible change. The ceria lattice parameters, on the other hand, seem to be somewhat smaller than expected for pure CeO_2, suggesting some zirconium incorporation into the CeO_2 lattice. However, due to the strong peaks overlapping and the weak intensity of the ceria signal, the XRD data cannot undoubtedly indicate if any zirconium was incorporated and to what extent. The XRD observations indicate a substantial stability of the ZrO_2-1 support but significant structural changes for ZrO_2-2, which relate well to the modifications in the total surface area (Table 1) and pore size distribution (Fig. 4). As the neat ZrO_2 supports, i.e. not impregnated,
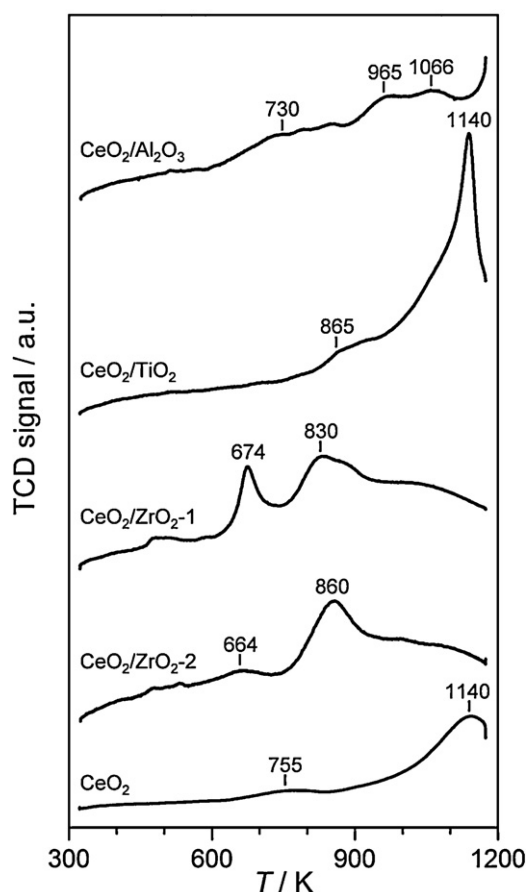
Fig. 7. H_2-TPR profiles of bulk ceria and supported CeO_2 catalysts, normalized by the Ce content.

Fig. 8. Raman spectra of CeO_2, ZrO_2-1, CeO_2/ZrO_2-1, and CeO_2/ZrO_2-2 (solid lines). For the two catalysts, fitting curves of ZrO_2 (dash-dotted lines), CeO_2 (dashed line), and Ce–Zr mixed phases (solid line) are displayed.

preserved their structural properties under the same conditions as applied for the calcination of the as-prepared catalysts, the change from the monoclinic to the tetragonal phase was likely triggered by the presence of CeO_2 or its precursor. Further considerations on this intriguing but complex phenomenon are proposed in the next paragraph. Overall, the XRD results are in line with the porosity results and indicate that the size of the ceria nanostructures varies depending on the carrier.

The reducibility of the catalysts was investigated by H_2-TPR (Fig. 7). The reduction curve of bulk CeO_2 calcined at 1173 K (low surface area) is shown for comparative purposes. As the supports are hardly reducible in the explored temperature range, the features distinguishable in the profiles are related to the reduction of the Ce-containing species. For CeO_2/Al_2O_3, weak peaks at 730, 965, and 1066 K and a more intense peak starting at 1203 K are detected. The signals below 1000 K refer to the reduction of small and well-dispersed CeO_2 crystallites and to CeO_2 particles strongly interacting with Al_2O_3, while those above 1000 K are attributed to the reduction to $CeAlO_3$ which is formed during the H_2-TPR analysis [23,35]. For the titania-supported catalyst, the reduction profile is dominated by a narrow and very intense signal at 1140 K accompanied by a weak and broad feature centered at 865 K. These peaks likely originate from the surface and bulk reduction of large CeO_2 particles. In fact, (i) the reduction pattern resembles that of bulk ceria, (ii) the diffractogram of this catalyst exhibits sharp CeO_2 reflections, (iii) and large CeO_2 particles have been visualized by TEM (*vide infra*). The profile of the ZrO_2-1-supported material exhibits two distinct peaks of similar intensity at 674 K and 830 K. The former can be related to surface reduction of Ce–Zr mixed oxides or CeO_2 nanostructures, while the latter falls in the
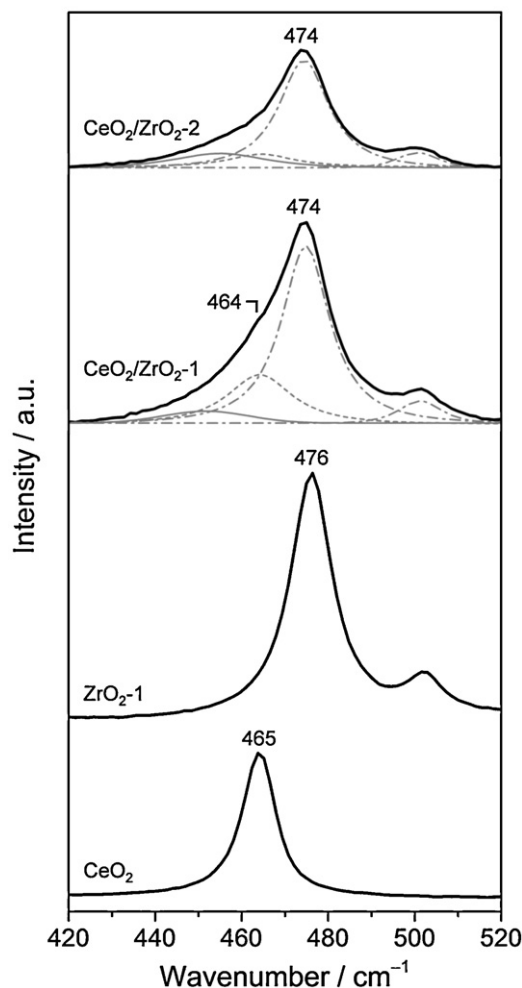
reduction range of bulk Ce–Zr mixed oxides nanostructures [32,36]. CeO_2/ZrO_2-2 renders similar features. Still, the low-temperature signal is much weaker and the high-temperature peak more pronounced and slightly shifted to higher temperature (860 K) (Fig. 7). Thus, CeO_2/ZrO_2-1 seems to contain both Ce–Zr mixed phases and pure ceria, while CeO_2/ZrO_2-2 predominantly possesses Ce–Zr mixed phases. In view of these findings, it is speculated that ZrO_2-2, due to the originally higher surface area, interacts more extensively with ceria than ZrO_2-1, which determines a larger degree of Zr incorporation in the CeO_2 lattice, and, possibly, a higher instability towards a phase change. Based on the H_2-TPR results, the different HCl oxidation activity of the catalysts can be preliminary understood based on the size, chemical nature, and dispersion of the Ce-based structures stabilized by the supports. The superiority of the zirconia-supported samples seems to originate from the presence of small nanostructures of CeO_2, ensuring high dispersion, and, possibly, of Ce-Zr mixed phases, which are known to possess a higher oxygen storage capacity than pure CeO_2 [6]. The improved performance of CeO_2/ZrO_2-1 compared to CeO_2/ZrO_2-2 is tentatively rationalized considering that (i) surface Ce atoms are needed for the reaction besides oxygen vacancies [4] and their binding properties might be negatively impacted to some extent when it is incorporated in a solid solution with ZrO_2 and (ii) that the mixed phase is more abundant in CeO_2/ZrO_2-2. As the alumina-supported ceria phase appear to have a high dispersion, the inferior performance of the CeO_2/Al_2O_3 catalyst might relate to the absence

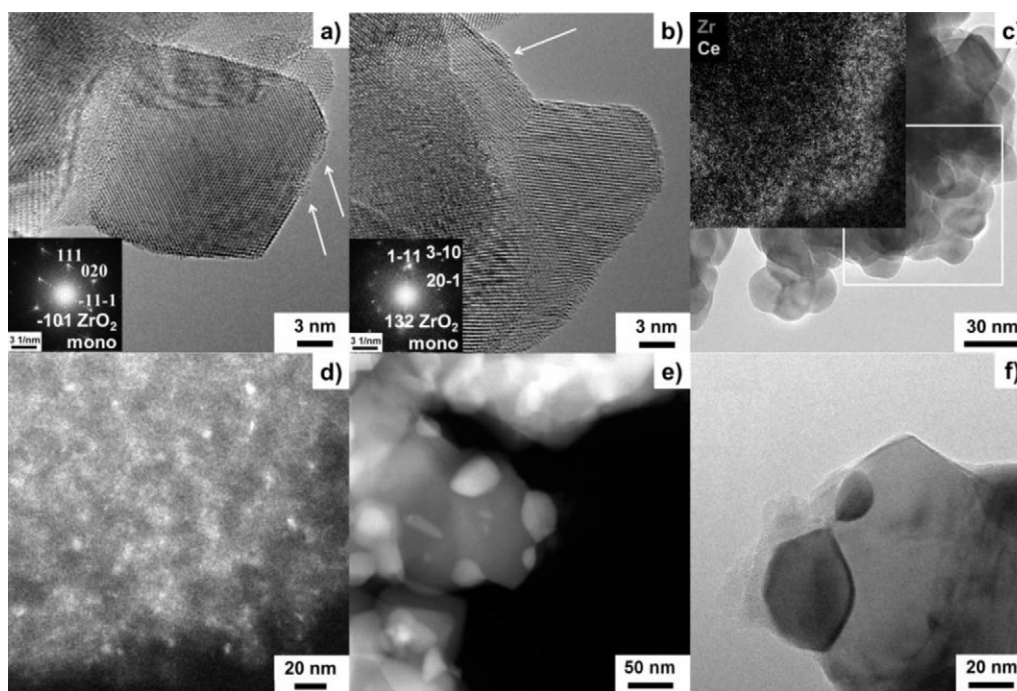**Fig. 9.** HRTEM images of (a) fresh and (b) used CeO_2/ZrO_2-1, (c) EFTEM and EELS (inset) map of fresh CeO_2/ZrO_2-1; (d) DFTEM of fresh CeO_2/Al_2O_3; and (e) STEM and (f) TEM images of fresh CeO_2/TiO_2.

of electronic effects induced by the support, as suggested by the kinetic analyses (Section 3.1). The limited activity of CeO_2/TiO_2 can be traced back to the presence of CeO_2 as particles of considerably large size, *i.e.* to a low dispersion of ceria.

As a well-established technique for the characterization of $CeZrO_x$ solid solutions, Raman spectroscopy was applied to further study CeO_2/ZrO_2-1 and CeO_2/ZrO_2-2 in order to support the presence of intermixed ceria-zirconia phases. It is worth mentioning that the characterization of our systems is particularly challenging as the extent of formation of intermixed phases is limited by the low overall Ce content ($\sim$7 wt.%) and the intermixing might only occur at the interface between ceria and zirconia, *i.e.* with only part of the ceria phase. Fig. 8 displays the Raman spectra of these catalysts, as well as of bulk ceria calcined at 1173 K and ZrO_2-1, as references. For sake of clarity, the spectrum of the ZrO_2-2 carrier was not included as perfectly superimposable to that of ZrO_2-1 in the spectral range reported. The slight shift of the zirconia signal at 476–474 cm^{-1} and its pronounced tailing towards lower wavenumbers might indeed point to the presence of ceria and Ce–Zr mixed oxides [37,38]. In fact, the spectrum of pure ceria is dominated by a sharp signal at 465 cm^{-1} and ceria-zirconia solutions render a strong peak between *ca.* 467 and 452 cm^{-1}, the more shifted to lower frequencies within this range the more abundant the amount of Zr [37,38]. At a closer look, the patterns of the two catalysts appear slightly different. Only for CeO_2/ZrO_2-1, a more defined shoulder at 464 cm^{-1} seems to stand out. Furthermore, the tailing for CeO_2/ZrO_2-2 is stronger at smaller wavenumbers. Upon fitting of the signals, it appears that the contributions due to ceria and mixed Ce–Zr phases are indeed different. For CeO_2/ZrO_2-1, pure ceria dominates over the mixed Ce–Zr phase, while the Ce–Zr mixed phase seem to be more abundant in CeO_2/ZrO_2-2. According to the maxima of their fitted curves (450 and 454 cm^{-1} for CeO_2/ZrO_2-1 and CeO_2/ZrO_2-1, respectively), the Ce–Zr mixed phases seem to be rich in Zr, especially in the case of CeO_2/ZrO_2-1 [38]. Overall, these results are in line with the H_2-TPR data.

Further studies were undertaken by transmission electron microscopy. For this purpose, CeO_2/Al_2O_3 with 12.2 wt.% Ce was investigated, since its activity is more relevant and the linearity obtained between the HCl conversion and the Ce loading let us suppose that the morphology of the supported phase does not remarkably change with the loading. For the fresh CeO_2/ZrO_2-1 sample, the mean particle size of ZrO_2-1 was $\sim$20 nm, which was not significantly altered upon HCl oxidation. HRTEM was used to analyze the crystalline structure of the samples. In agreement with XRD, monoclinic ZrO_2 (ICSD 89426) was found as the dominant structure, and the presence of tetragonal ZrO_2 (ICSD 23928) and cubic CeO_2 (ICDS 29046) was verified. The amount of CeO_2 particles found on the fresh and used samples was significantly lower than expected from the relatively high metal loading. Lattice analysis from the high-resolution micrographs was not able to confirm the presence of a solid solution of CeO_2 and ZrO_2. This can be attributed to the fact that the lattice variations may occur in a range that lies within the error bars of the TEM lattice analysis. Mixed Ce-Zr phases could be observed for example by Yashima et al. [39] for well-crystallized materials prepared *via* ceramic route only by use of neutron diffraction. A detailed investigation of the catalyst particles by HRTEM revealed that the surface of the monoclinic ZrO_2 particles shows a partial decoration with atomic clusters, as indicated by the arrows in Fig. 8a,b. The nature of the clusters was addressed by energy filtered images. The EELS maps generated using the Zr M and Ce N edges are shown in Fig. 9c. EFTEM mappings performed at several positions within the fresh and spent catalyst reveals that the Ce surface coverage on Zr is made of particles with various sizes (from clusters to nanoparticles), thus explaining the clusters observed in the micrographs of the fresh and used CeO_2/ZrO_2 samples. As mapping suggests a higher Ce content compared to that implied by the amount of CeO_2 detected by HRTEM, this may further hint to intermixing of the ceria phase with ZrO_2 to a certain extent. With regards to the fresh CeO_2/Al_2O_3, BF/DFTEM analyses suggest a relatively narrow size distribution of the CeO_2 particles varying from clusters of $\sim$3 nm up to 8 nm (Fig. 9d), with few bigger particles of up to 15 nm in diameter. No significant modifications were observed for the catalyst after use in HCl oxidation. For the fresh CeO_2/TiO_2, HAADF-STEM shows, owing to its Z sensitivity,

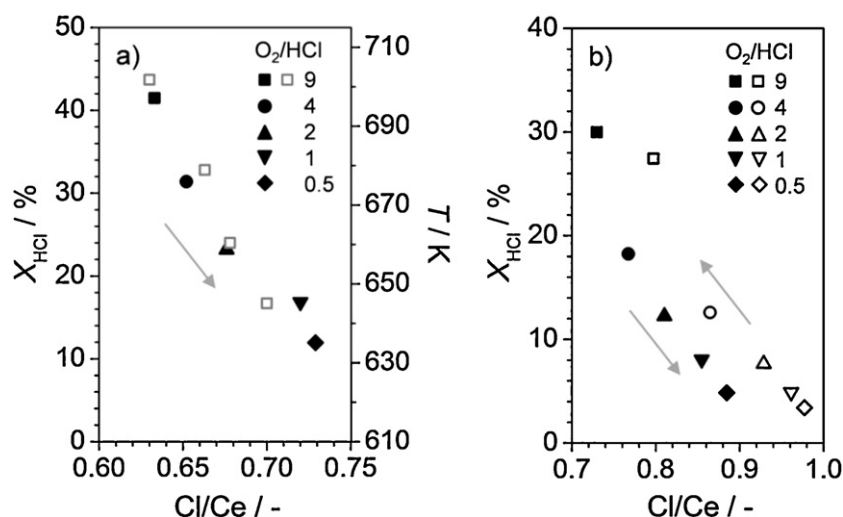**Fig. 10.** (a) HCl conversion *versus* molar Cl/Ce ratio over CeO_2/ZrO_2-1, $W_{cat} = 0.7$ g, at 643–703 K and $O_2/HCl = 9$ (open squares), as well as $O_2/HCl = 0.5–9$ at 703 K (downwards, solid symbols). (b) HCl conversion *versus* molar Cl/Ce ratio over CeO_2/Al_2O_3, $W_{cat} = 0.5$ g, at 703 K and $O_2/HCl = 0.5–9$ (upwards, open symbols; downwards, solid symbols).

bright CeO_2 particles of 20–50 nm size on the darker TiO_2 support grains (Fig. 9e). The result is confirmed by HRTEM (Fig. 9f). The similar morphology of both CeO_2/ZrO_2-1 and CeO_2/Al_2O_3 in fresh and used forms indicates high stability under reaction conditions, thus strengthening the relevance of the structure-function relationships derived so far in this work.

3.3. In situ PGAA studies

In situ PGAA was utilized to evaluate the effect of Cl uptake during HCl oxidation over CeO_2/ZrO_2-1 (7 wt.% Ce) and CeO_2/Al_2O_3 (12.2 wt.% Ce) (Fig. 10). Both the influence of temperature and partial pressure of oxygen were explored. According to recent experiments with bulk ceria, a higher temperature and mixtures with higher O_2/HCl ratios gave rise to lower Cl uptake and, concomitantly, higher reactivity [5]. The results obtained with the supported samples confirmed these trends. Measurements with CeO_2/ZrO_2-1 even suggest that the Cl coverage is a key negative parameter governing the actual reactivity (Fig. 10a). Thus, higher temperature reduces site blocking by surface chlorine. Although this effect is formally similar to that found with bulk ceria, the lower apparent activation energy observed with CeO_2/ZrO_2-1 indicates that Cl blocking at lower temperature is somewhat less efficient, likely due to electronic modification imparted by the strong interaction with zirconia. Bulk chlorination, giving rise to unsteady Cl/Ce ratios at $O_2/HCl < 2$ [5], was not investigated directly here, but the results in Fig. 10a suggest this not to be significant for CeO_2/ZrO_2-1. Conversely, CeO_2/Al_2O_3 evidently suffered from bulk chlorination (Fig. 10b). In the O_2/HCl variation experiments, when starting with oxidizing or with chlorinating conditions, both the reactivity (Fig. 2a) and the chlorination degree (Fig. 10b) were affected and the catalyst after bulk chlorination exhibited worse performance. This refers to the clear negative influence of subsurface/bulk chlorination. The stronger positive reaction order for oxygen with CeO_2/Al_2O_3 indicates an increased inhibition by adsorbed Cl as compared to CeO_2/ZrO_2-1. This was most pronounced for the upward series of CeO_2/Al_2O_3 (open symbols in Figs. 2a and 10b). Therefore, we can conclude that CeO_2/Al_2O_3 essentially functions as unsupported ceria, though with small particles, and more severe Cl inhibition, whereas ZrO_2-1 should have induced some subtle modification in the reactants binding, resulting into a more efficient catalyst.

4. Conclusions

In this study, we have undertaken the search of an adequate support for ceria, recently indicated as promising alternative active phase to RuO_2 for the catalytic oxidation of HCl. Our work included material preparation using three conventional types of support (ZrO_2, Al_2O_3 and TiO_2), catalytic activity testing, and characterization. Zirconia-supported catalysts emerged as the best performers. Kinetic investigations revealed comparable or improved features with respect to bulk ceria and testing in a pilot reactor using pellets of a CeO_2/ZrO_2 catalyst with optimized metal content proved its long-term stability. CeO_2/Al_2O_3 was moderately active and CeO_2/TiO_2 exhibited limited activity. The copresence of nanostructures of CeO_2 and a Ce–Zr mixed oxide phase, which offer high dispersion, enhanced oxidation properties, and reduced chlorination is the key for the superior performance of CeO_2/ZrO_2. In spite of the high dispersion of ceria over alumina in form of nanoparticles, the inferior activity of this catalyst derives from the likely stronger Cl binding to the nanoparticles and the absence of electronic effects associated with the support. In the case of CeO_2/TiO_2, the dramatic sintering of the carrier during thermal activation of the as-impregnated catalyst hinders an effective deposition of the active phase, which appears in form of large particles. Based on these results, CeO_2/ZrO_2-1 stands as a cost-effective, eco-friendly, and industrially relevant catalyst for chlorine recycling, challenging the present dominance of RuO_2-based catalysts. This catalyst can also be retrofitted in the few existing plants.

Acknowledgements

References

[1] J. Pérez-Ramírez, C. Mondelli, T. Schmidt, O.F.K. Schlueter, A. Wolf, L. Mleczko, T. Dreier, Energy and Environmental Science 4 (2011) 4786–4799.
[2] T. Hibi, H. Nishida, H. Abekawa, US 5,871,707 (1999).
[3] A. Wolf, L. Mleczko, O.F. Schlüter, S. Schubert, EP 2026905 (2006).
[4] A.P. Amrute, C. Mondelli, M. Moser, G. Novell-Leruth, N. Lopez, D. Rosenthal, R. Farra, M.E. Schuster, D. Teschner, T. Schmidt, J. Pérez-Ramírez, Journal of Catalysis 286 (2012) 287–297.
[5] R. Farra, M. Eichelbaum, R. Schlögl, L. Szentmiklósi, T. Schmidt, A.P. Amrute, C. Mondelli, J. Pérez-Ramírez, D. Teschner, Journal of Catalysis (2012), http://dx.doi.org/10.1016/j.jcat.2012.09.024.
[6] A. Trovarelli, Catalysis Reviews-Science and Engineering 38 (1996) 439–520.

[7] R.J. Gorte, AIChE Journal 56 (2010) 1126–1135.
[8] Q. Fu, H. Saltsburg, M. Flytzani-Stephanopoulos, Science 301 (2003) 935–938.
[9] A. Primo, T. Marino, A. Corma, R. Molinari, H. Garcia, Journal of the American Chemical Society 133 (2011) 6390–6933.
[10] Y.S. Chaudhary, S. Panigrahi, S. Nayak, B. Sarpati, S. Bhattacharjee, N. Kulkarni, Journal of Material Chemistry 20 (2010) 2381–2385.
[11] M. Mogensen, N.M. Sammes, G.A. Tompsett, Solid State Ionics 129 (2000) 63–94.
[12] B. Zhu, M.D. Mat, International Journal of Electrochemical Science 1 (2006) 383–402.
[13] F. Zhou, X. Zhao, H. Xu, C. Yuan, Journal of Physical Chemistry C 111 (2007) 1651–1657.
[14] S. Colussi, C. de Leitenburg, G. Dolcetti, A. Trovarelli, Journal of Alloys and Compounds 374 (2004) 387–392.
[15] S. Carrettin, P. Concepción, A. Corma, J.M. López Nieto, V.F. Puntes, Angewandte Chemie International Edition 43 (2004) 2538–2540.
[16] A. Gómez-Cortés, Y. Márquez, J. Arenas-Alatorre, G. Díaz, Catalysis Today 133 (2008) 743–749.
[17] A. Martínez-Arias, A.B. Hungría, G. Munuera, D. Gamarra, Applied Catalysis B 65 (2006) 207–216.
[18] W. Shin, C. Jung, J. Han, S. Nam, T. Lim, S. Hong, H. Lee, Journal of Industrial and Engineering Chemistry 10 (2004) 302–308.
[19] T.X.T. Sayle, S.C. Parker, C.R.A. Catlow, Surface Science 316 (1994) 329–336.
[20] A. Trovarelli, C. de Leitenburg, M. Boaro, G. Dolcetti, Catalysis Today 50 (1999) 353–367.
[21] S.M. Saqer, D.I. Kondarides, X.E. Verykios, Applied Catalysis B 103 (2011) 275–286.
[22] A. Martínez-Arias, M. Fernández-García, L.N. Salamanca, R.X. Valenzuela, J.C. Conesa, J. Soria, Journal of Physical Chemistry B 104 (2000) 4038–4046.
[23] S. Damyanova, C.A. Perez, M. Schmal, J.M.C. Bueno, Applied Catalysis A 234 (2002) 271–282.
[24] J. Kašpar, P. Fornasiero, M. Graziani, Catalysis Today 50 (1999) 285–298.
[25] Y. Madier, C. Descorme, A.M. Le Govic, D. Duprez, Journal of Physical Chemistry B 103 (1999) 10999–11006.
[26] B.M. Reddy, A. Kahn, P. Lakshmanan, M. Aouine, S. Loridant, J.-C. Volta, Journal of Physical Chemistry B 109 (2005) 3355–3363.
[27] B.M. Reddy, A. Kahn, Langmuir 19 (2003) 3025–3030.
[28] R.W. Cheary, A. Coelho, Journal of Applied Crystallography 25 (1992) 109–121.
[29] D. Balzar, in: R.L. Snyder, J. Fiala, H.J. Bunge (Eds.), Defect and Microstructure Analysis by Diffraction, International Union of Crystallography Monographs on Crystallography, vol. 10, Oxford University Press, New York, 1999, pp. 94–124.
[30] D. Teschner, R. Farra, L. Yao, R. Schlögl, H. Soerijanto, R. Schomäcker, T. Schmidt, L. Szentmiklósi, A.P. Amrute, C. Mondelli, J. Pérez-Ramírez, G. Novell-Leruth, N. López, Journal of Catalysis 285 (2012) 273–284.
[31] A.P. Amrute, C. Mondelli, M.A.G. Hevia, J. Pérez-Ramírez, Journal of Physical Chemistry C 115 (2011) 1056–1063.
[32] P. Fornasiero, G. Balducci, R. Di Monte, J. Kašpar, V. Sergo, G. Gubitosa, A. Ferrero, M. Graziani, Journal of Catalysis 164 (1996) 173–183.
[33] J. Lin, J.C. Yu, Journal of Photochemistry and Photobiology A 116 (1998) 63–67.
[34] D.A.H. Hanaor, C.C. Sorrell, Journal of Materials Science 46 (2011) 855–874.
[35] A. Piras, S. Colussi, A. Trovarelli, V. Sergo, J. Llorca, R. Psaro, L. Sordelli, Journal of Physical Chemistry B 109 (2005) 11110–11118.
[36] G.R. Rao, B.G. Mishra, Bulletin of the Catalysis Society of India 2 (2003) 122–134.
[37] A. Trovarelli, F. Zamar, J. Llorca, C. de Leitenburg, G. Dolcetti, J.T. Kiss, Journal of Catalysis 169 (1997) 490–502.
[38] G. Postole, B. Chowdhury, B. Karmakar, K. Pinki, J. Banerji, A. Auroux, Journal of Catalysis 269 (2010) 110–121.
[39] M. Yashima, T. Hirose, S. Katano, Y. Suzuki, M. Kakihana, M. Yoshimura, Physical Review B 51 (1995) 8018–8025.